

Construction of MoS₂/graphite/C₃N₄ Ternary Photocatalytic System Through Communicating Electron and Holes Transferring by Graphite and its Application for Dye Wastewater Photocatalytic Treatment Under Visible Light

¹Ting Cheng, ²Chen Chen*, ²Lei Wang, ¹Weifang Xie, ²Dianyi Wu, ^{1,3}Xiao Zhang
²Zhiyi Zhou and ²Xiaoqin Zhang²

¹*School of Environmental Ecology, Jiangsu City Vocational College, Nanjing, 210017, China;*

²*School of Environmental and Chemical Engineering, Jiangsu University of Science and Technology, Zhenjiang, 212100, China;*

³*Nanjing University and Yancheng Academy of Environmental Technology and Engineering, Yancheng 224000, China.*
chenc@just.edu.cn*

(Received on 12 August 2021, accepted in revised form 28th January 2022)

Summary: A MoS₂/graphite/C₃N₄ ternary photocatalytic material (MGC catalyst) was successfully synthesized, characterized, and applied to the photodegradation of Methylene Blue (MB). In addition, the photocatalytic mechanism of MGC was illustrated through modern characterization technology and density functional theory (DFT) computation. The findings of characterization (XRD, SEM-EDX, UV-Vis, XPS) confirmed that MGC was a composite photocatalyst of C₃N₄-graphite-MoS₂ ternary structure, and displayed excellent visible light absorption performance. MGC photocatalyst exhibited the highest degradation efficiencies of MB than that of C₃N₄ and MoS₂ catalyst, and it effectively improved the removal of pollutant. Also, the first-order reaction model suitably described the photocatalytic reaction process. The recycling experiments proved that MGC catalyst possessed remarkable photocatalytic stability in the degradation activities of MB, and the morphology maintained stable after three times of reusing. The ternary composite structure of MGC was conducive to the generation and transfer of the photo-generated electrons and photo-generated holes. Besides, MGC photocatalyst obtained the lowest photoluminescence spectrum intensity, which might decrease the combination probability of photo-induced electrons and holes. Electron spin resonance (ESR) analysis verified that the active radicals of •OH and •O₂⁻ measured in photocatalytic reaction probably played an essential part in the degradation of MB. Furthermore, through calculating the band structure, density of states (DOS), and work function, it was illustrated that the two opposite potential barriers forming between graphite, MoS₂ and C₃N₄ interface effectively accelerated the division of photo-induced electrons and photo-induced holes in MoS₂ and C₃N₄. Then, the recombination probability of photo-induced electrons and holes was reduced, and hence that greatly improved the photocatalytic efficiency of MB.

Keywords: Photocatalysis; C₃N₄; MoS₂; Z-scheme photocatalyst; DFT calculation.

Introduction

Every year, million tons of industrial organic wastewater is produced in chemical industrial companies. This kind of organic wastewater is generally discharged from industries such as papermaking, leather, dyes, and food [1]. The wastewater contains a lot of carbohydrates, fats, proteins, cellulose, and other organic matters [2]. If discharged directly, it will cause serious pollution to human health and ecological environment. Hence, effective ways are crucial to treat such organic wastewater. So far, there are many techniques to treat organic wastewater, including biological degradation [3, 4], chemical methods [5], adsorption [6-8], membrane separation [9], advanced oxidation [10, 11], photocatalysis [12, 13], photocatalysis coupled with electricity production technology [14, 15]. Among these techniques, effective and economical processing methods have always attracted the attention of many researchers. Generally, traditional treatment

techniques for organic wastewater have several shortcomings. In addition, based on the generation of free radicals and the conditions of reaction, advanced oxidation technology includes catalytic wet air oxidation [16, 17], electrochemical oxidation [18, 19], Fenton oxidation [20, 21], and photocatalysis [22-24].

Photocatalysis is a new type of wastewater treatment process that developed in the last century, and arouses much attention in these years. According to references, photocatalysis is an efficient and safe environment-friendly environmental purification technology, and it utilizes the photo-generated electrons and photo-generated holes produced by photocatalyst to take action in the oxidation and reduction reaction, and then degrades various pollutants, including organic substances [25, 26]. Normally, the photocatalytic reaction takes semiconductor materials as the catalyst. Under the

*To whom all correspondence should be addressed.

excitation of light, electrons in the semiconductor material transition from the position of valence band to the position of conduction band, and forming photo-produced electrons in the position of conduction band and photo-produced holes in the position of valence band [27]. It was reported that single photocatalysts displayed relatively limited degradation efficiencies for pollutant because of their single energy band structures, higher electron-hole recombination rates, and other factors. In this case, the development of composite photocatalysts has attracted more and more attention from researchers [28, 29]. Wang et al utilized $\text{MoSe}_2/\text{Bi}_2\text{S}_3/\text{CdS}$ hollow structure as dual Z-Scheme heterojunction to increase the utilization rate of light source, and the material also exhibited excellent photocatalytic activity in the hydrogen evolution and removal of Cr (VI) and 2,4,6-trichlorophenol [30]. Zhu and Zhou synthesized nitrogen doped $g\text{-C}_3\text{N}_4$, the material displayed extremely narrow band gap, which enhanced the absorption of visible light and promoted the photocatalytic activity [31]. Chen et al synthesized Ag doped NaSbO_3 photocatalyst (ANS) with greatly reduced the band gap, and ANS displayed excellent visible light absorption performance [32]. Generally speaking, photocatalytic materials can be mainly divided into oxides, sulfides, nitrides and phosphides and the phosphide, such as TiO_2 [33-35], ZnO [36-39], BiVO_4 [12, 40], ZrO_2 [41, 42], CdS [43, 44], C_3N_4 [45-47], MoS_2 [48, 49], WO_3 [50, 51]. Although these photocatalysts have favorable catalytic properties, there are still many problems to solve, such as the stability of catalysts (photoetching phenomenon), the problem of light absorption (mainly ultraviolet absorption), and the environmental toxicity of catalysts [52].

Carbon nitride (C_3N_4), a new kind of non-metal semiconductor polymer, is used in photocatalytic environment because of the distinctive chemical and electronic energy band structure, high physical and chemical stability, and its economic and environmental characteristics [46, 53]. It has great potential in photocatalytic environmental purification, hydrogen production by water decomposition and photoelectric conversion [54, 55]. However, C_3N_4 catalyst itself still has some problems, such as its specific surface area is low, the absorption of visible light is limited, the recombination of photogenerated carriers is rapid, etc., which severely restrict its photocatalytic performance. Therefore, how to further improve its photocatalytic performance develops one of the hot problems. Among photocatalyst materials, molybdenum sulphide (MoS_2) has good application prospects in the photocatalytic hydrogen production because of its outstanding electronic, optical,

mechanical, and thermal characteristics [56]. Nevertheless, MoS_2 requires a co-catalyst to achieve photocatalytic water decomposition for the preparation of hydrogen under sunlight. Hence, the construction of a molybdenum disulfide-based composite catalyst might be a valid method to enhance the photodegradation effect, and that is of great significance to photocatalysts [57].

According to the related literatures, among the composite photocatalyst techniques (the doping of elements, p-n heterojunctions, Z-scheme type of photocatalysts, etc.), Z-scheme composite method may be one of the most potential photocatalyst composite strategies. Z-scheme type of composite technique is the energy figure for the transfer of photo-produced carrier forming like a letter of "Z". It was reported that Z-scheme photocatalytic materials greatly enhanced the separation probability of photo-produced electrons and photo-produced holes, and accelerated the redox ability of photo-produced electron and photo-produced holes, and then improved the photocatalytic efficiency of pollutants [58, 59]. According to the material properties of C_3N_4 and MoS_2 mentioned above, if we develop a ternary composite photocatalytic material based on these two materials, it is likely to achieve the effective photocatalytic performance of organic substances under visible light through separating the photo-generated electrons and holes.

In our work, the ternary composite photocatalyst of $\text{MoS}_2/\text{graphite}/\text{C}_3\text{N}_4$ (MGC catalyst) was successfully constructed, synthesized, and characterized by many modern instruments, mainly including the morphology, chemical and optical properties of material. Also, we utilized the Methylene Blue (MB) to verify the photocatalytic effect of MGC catalyst. The impact factors, such as catalyst dosages, whether to provide visible light, and the reaction kinetics were studied at the same time. Moreover, the photocatalytic degradation performance and the morphology of recycling usage of MGC catalyst were evaluated in experiments. To clarify the photocatalytic mechanism of MGC catalyst, the solid photoluminescence (PL), the Electron spin resonance (ESR), and electrochemical analysis were conducted. Besides, the software of Vienna Ab initio Simulation Package (VASP) and the theory computation of spin-polarized Density Functional Theory (DFT) were also carried out to illustrate the action of photo-produced electrons and photo-produced holes. The various experimental and theoretical computation findings demonstrated that MGC catalyst exhibited outstanding photocatalytic activity for the organic substance degradation in solution. Additionally, these

findings were highly recommended to develop more suitable and effective photocatalytic materials to degrade organic substances, and alleviate the environmental pressure caused by organic pollutions.

Experiments

Synthesis of photocatalyst

The synthesis method of C_3N_4 was basically the same as that in the literature [60], and the two-stage heating method was used. Typically, 15 g of melamine was put at a covered crucible, and heated to the temperature of 550 °C with a ramp speed of 5°C/min in the muffle furnace. Then, the temperature was kept at 550 °C for 3 hours. When cooled to the room temperature naturally, we obtained the first calcination product. The secondary calcination was performed with a similar approach, and the procedures were as follows: the first calcination product was continued to be heated at 520°C with a heat rate of 5°C/min. The heating temperature was maintained for 2 hours, and then cooled to the room temperature again, and C_3N_4 catalyst was obtained.

In addition, the synthesis method of MoS_2 was as follows: dissolving 1.2g of sodium molybdate ($Na_2MoO_4 \cdot 2H_2O$) and 1.6g of thiourea (CH_4N_2S) in 80mL of distilled water, stirring for 1 hour with a magnetic mixer, and then the mixed solution was put in the high pressure autoclave with PTFE material lining. The experiment was conducted at the temperature of 160°C, and maintained for 24 hours. After that, we used alcohol and distilled water washed the reaction substance for many times, and the reaction substance was centrifuged using a low-speed centrifuge, and dried using a blast drying oven, then the MoS_2 catalyst was obtained.

Dissolved 1.2g of sodium molybdate ($Na_2MoO_4 \cdot 2H_2O$) and 1.6g of thiourea (CH_4N_2S) in 80mL of distilled water, stirred evenly, and then added 1g of graphite and 1g of C_3N_4 to the reaction system. Then, the mixture liquid was put into a high-pressure reactor lined with polytetrafluoroethylene, and then stirred with magnetic stirrer for 1 hour. The reaction was conducted at the temperature of 160°C for 24 hours. Afterwards, the reaction substance was centrifuged using a low-speed centrifuge, and alcohol and distilled water was used to wash it until neutral. And then, the reaction product was dried by blast drying oven, and the MGC catalyst was obtained.

Materials characterization

To illustrate the various properties of synthesized material, catalysts were characterized by many modern instruments, mainly containing X-ray diffraction (XRD), UV-vis diffuse reflectance spectra (DRS), Scanning electron microscopy-energy dispersive spectroscopy (SEM-EDX), X-ray photoelectron spectroscopy (XPS), photoluminescence (PL), Electron spin resonance (ESR), electrochemical impedance spectroscopy (EIS) and electrochemical photocurrent (interval 20s). In the characterization of synthesized material, a HITACHI(S-3400N) scanning electron microscope was used to observe the morphologies of product; a Shimadzu XD-3A diffractometer was used to measure the XRD patterns of powder samples, and utilizing the radiation of $Cu-K\alpha$ ($\lambda = 1.54056\text{\AA}$); a PHI 5000 VersaProbe XPS equipment was utilized to examine the X-ray photoelectron spectroscopy spectra; a PerkinElmer Ultraviolet spectrophotometer was measured the UV-vis spectra; a HITACHI Fluorescence spectrometer (F-7000) was analyzed the solid photoluminescence; a Electron paramagnetic resonance spectrometer (EMXmicro-6/1/P/L, Karlsruhe, Germany utilizing) was used to measure the Electron spin resonance; a CHI 660E electrochemical workstation was measured the electrochemical impedance spectroscopy and photocurrent. In addition, the DMPO (5, 5-dimethyl-1-pyrroline N -oxide) was choose as the trapping agent for the free radical of $\bullet O_2^-$ and $\bullet OH$.

Photocatalytic experiments

In experiments, MB and tetracycline were used as pollutants to investigate the photodegradation effect of photocatalyst under the irradiation of visible light (300W Xe-lamp). In every test, photocatalyst (0.020g for MB) was put into 30ml of MB solution to keep the initial concentration was 10 mg/L. All photocatalytic experiments were carried out at room temperature (25°C), and the reaction liquids were put into a transparent photocatalytic reaction vessel. The photocatalytic reaction time was from -10 to 30 minutes, and the visible light was turn at 0 minute. After the photocatalytic degradation experiment, Ultraviolet visible spectrophotometer was used to measure the remnant concentration of MB at 662nm.

In our research, to illustrate the photocatalytic mechanism of this reaction, the active species produced in the photocatalytic reaction were analyzed, and different types of capturing agents were put into the mixtures to quench the reactive species. These scavengers included 0.037g of

EDTA-2Na, 0.0094g of TBA (*tert*-butyl alcohol), 0.0108g of BQ (1,4-benzoquinone) and 0.0142g of CCl_4 . In addition, to evaluate the photocatalytic properties of recycled photocatalyst, the consecutive cycles were done to determine the photocatalytic efficiencies of MB, and the photocatalyst was reused for three times. After each recycled cycle, 0.45 μm filter membrane was used to filter the photocatalyst from the reaction solution, and the recycled photocatalyst were then washed by deionized water for several times. After that, the recycled sample was dried to a constant weight at 75 $^\circ\text{C}$ in a blast drying oven for the next usage.

DFT calculation

In our research, Vienna Ab initio Simulation Package (VASP) software and spin-polarized Density Functional Theory (DFT) were carried out the DFT calculation to investigate the mechanism of photocatalytic reaction process. The exchange-correlation potential was computed by

Perdew-Burke-Ernzerhof functional (PBE) within the generalized gradient approximation (GGA) method. Also, the cut-off energy was 450eV and the K-points grids of dimensions were $5 \times 5 \times 5$ in the computed process. Fig.1 displayed the theory structure of crystal graphite, MoS_2 and C_3N_4 , the surface model of graphite, MoS_2 and C_3N_4 . In addition, we calculated the band structure using crystal model of graphite (Fig.1a), MoS_2 (Fig.1b), and C_3N_4 (Fig.1c). We also computed the work function through the surface model of model of graphite (Fig.1e), MoS_2 (Fig.1f) and C_3N_4 (Fig.1g). The vacuum slab of surface model was designed as 30 \AA for graphite, MoS_2 and C_3N_4 . First of all, both the atomic coordinates and cell parameters of graphite, MoS_2 , and C_3N_4 were optimized during the process of calculation, respectively. Besides, the theoretical crystal structure of graphite was a cell unit, including 16C atoms. The theoretical crystal structure of MoS_2 was a unit of cell, containing 8Mo and 16S atoms, and the theoretical crystal structure of C_3N_4 was a unit of cell, containing the atoms of 8N and 6C.

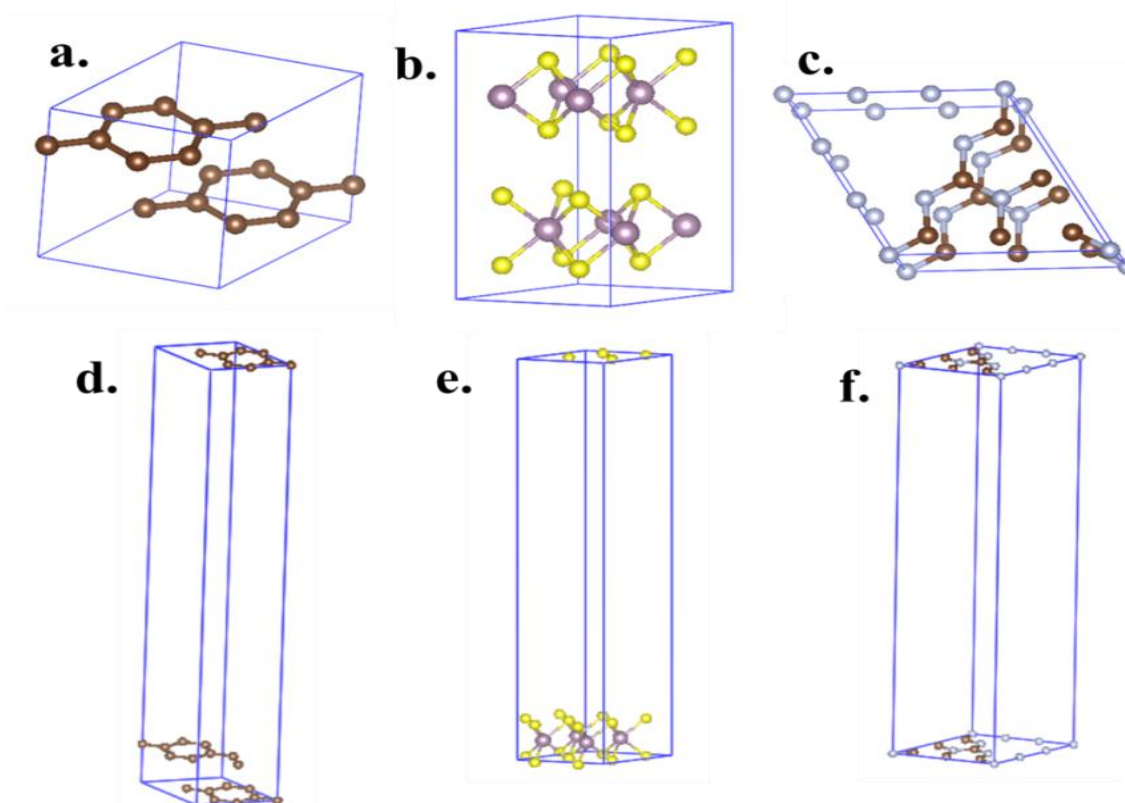


Fig.1: The theory structure of crystal model graphite (a), MoS_2 (b) and C_3N_4 (c), and the theory structure of surface model (for work function calculation) graphite (d), MoS_2 (e) and C_3N_4 (f), (the atom of C is coffee ball, the atom of S is yellow ball, the atom of Mo is violet ball, the atom of N is grey ball).

Results and discussions

XRD

Fig. 2 depicted XRD patterns of MGC, MoS₂, C₃N₄ and GCA. The main curves of GCA appeared at 2θ, 26.5°, 42.3°, 44.5°, 54.6°, and 77.4°, and these peaks were consistent with the standard curves of Graphite (PDF#41-1487). Also, for C₃N₄, the strong peaks around 2θ was ranged from 25.2° to 29.1°, indicating the existence of C₃N₄ (PDF#87-1526) [51]. Besides, the main peaks of MoS₂ appeared at 2θ, 14.3°, 32.5°, 33.4°, 39.5°, and 58.2°, which were in accordance with the molybdenite-MoS₂ (PDF#37-1492). For the peaks of MGC photocatalyst, all the main curves of XRD patterns for MoS₂, C₃N₄, and GCA could be observed. This phenomenon implied that MGC photocatalyst was a composite material of MoS₂, C₃N₄, and GCA.

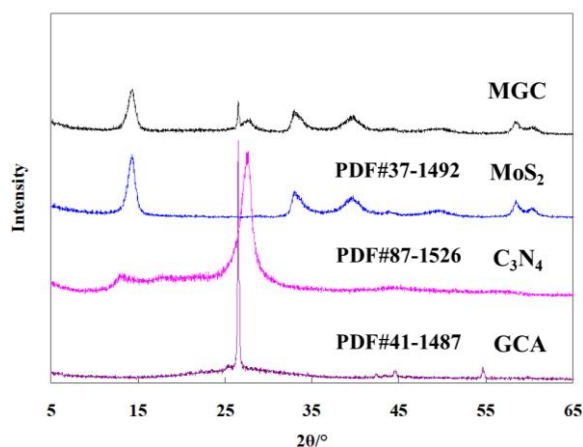


Fig. 2: XRD patterns of MGC, MoS₂, C₃N₄, and GCA.

UV-vis diffuse reflectance spectra

The results of UV-vis diffuse reflectance spectra were depicted in Fig.3. It could be seen that all C₃N₄ absorption bands were around from 300nm to 500nm, implying that C₃N₄ had excellent absorption for visible light with lower wavelength. In addition, both the absorption bands of MoS₂ and MGC were around from 300nm to 850nm. This result indicated both MoS₂ and MGC material had better absorption of visible light at all wavelengths.

As known, we often use Tauc equation (as below) to compute the band gap energy [12, 13].

$$\alpha(\nu)hv = A(h\nu - E_g)^{n/2} \quad (1)$$

where, α , h , ν , A and E_g expresses the absorption coefficient at light frequency ν , Planck constant, light frequency, a constant and band gap energy, respectively.

Based on the Tauc equation, E_g value can be gotten by depicting the curve of $[a(\nu)hv]^2$ versus $h\nu$ and extra-polating the linear part of the curve to the coefficient of zero absorption. In this work, we carried out this analysis and plotting process, as shown as Fig.3b. The band gaps energy of C₃N₄ and MoS₂ were 2.75eV and 1.46eV, respectively, and these values were very close to the results of other researchers [60, 61]. Besides, the band gap energy of MGC was also about 1.46eV. In this case, these analytical and fitting results implied that MGC material maintained lower band gap energy, which made MGC photocatalytic material also obtain excellent visible light absorption efficiency.

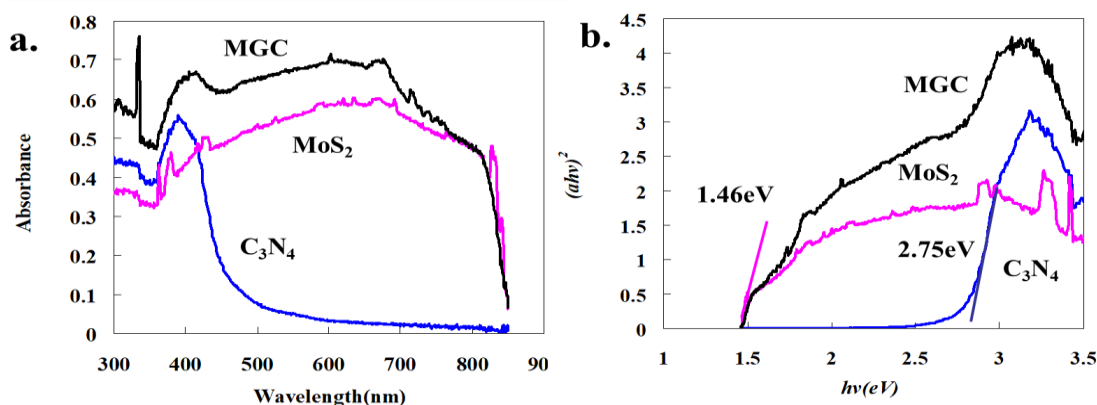


Fig. 3: UV-vis diffuse reflectance spectra for MGC, MoS₂, and C₃N₄ (a), and the plotting results of band gaps energy for MGC, MoS₂, and C₃N₄ (b).

SEM-EDX

Fig. 4 depicted the SEM analysis results of the original C_3N_4 , MoS_2 and graphite. The particle size of graphite particles in Fig.4e and Fig.4f was about from $3\mu m$ to $6\mu m$, and the microscopic morphology presented a stacked structure of flake particles. In addition, the thickness of the flaky particles was approximately in the range of 200nm to 300 nm, and the surface was relatively smooth, and such results were consistent with the typical graphite molecular crystal structure. Moreover, the analytical results of Fig.4c and Fig.4d displayed that the particle size of the larger MoS_2 particles was about $5\mu m$, while it was formed by agglomeration of a large number of random MoS_2 micro-particles (100-200nm). Besides, it was seen from Fig.4a and Fig.4b that C_3N_4 presented a fluffy, irregular structure, and a large number of nano- C_3N_4 particles (100-200nm) aggregated to form micron particles with a size of $3\mu m$ to $5\mu m$.

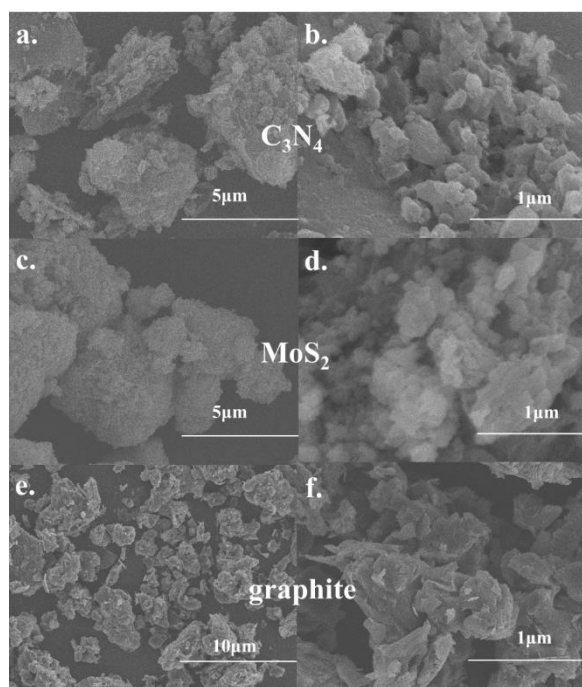


Fig. 4: SEM analytical results of original C_3N_4 , MoS_2 and graphite.

Fig. 5 depicted the SEM-EDX analysis results of MGC. It was appeared that in Fig.5a, a large number of flake structures could still be observed, that might be graphite particles in MGC material. Compared with Fig.4e and Fig.4f, the surface of flake particles in Fig.5a was no longer smooth, and the surface was covered by a large number of irregular small particles. Also, it could be more clearly observed from Fig.5b that the size of these particles

was around from 100nm to 200nm. Besides, further EDX analysis results showed that the element composition (mol/%) in the scanning area was C (57.98%), N (22.90%), S (12.90%), and Mo (6.22%). Additionally, the molar ratio of Mo and S elements was basically consistent with the composition of MoS_2 . Furthermore, according to the calculated results of molecular structure for C_3N_4 and the molar ratio for N element, the ratio of C element required to form C_3N_4 should be about 11.17%, and the excess C element might come from the flake graphite particles. Hence, it was proposed that a large number of nano-sized C_3N_4 and MoS_2 particles were attached to the surface of flake graphite particles after the synthesis reaction, forming a C_3N_4 -graphite- MoS_2 ternary structure.

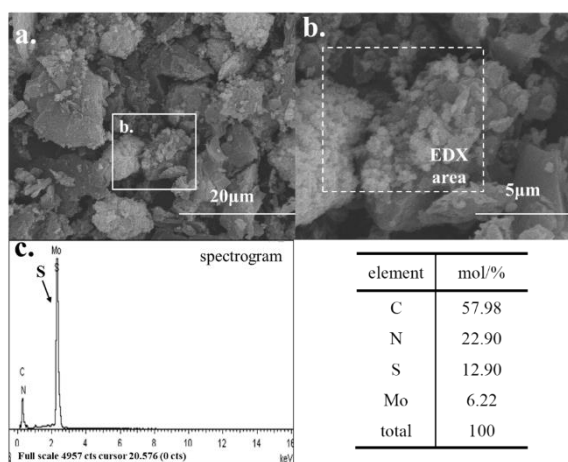


Fig. 5: SEM-EDX analytical results of original MGC.

XPS

Fig.6 further evaluated the surface chemical composition of MGC material through XPS. The main peaks of MGC appeared were $S2p$ (161eV), $Mo3d$ (229eV), $S2s$ (226eV), $C1s$ (288eV), $N1s$ (398eV), $Mo3p$ (394eV), and $Mo3s$ (531eV). All these elements could be found in MoS_2 , C_3N_4 and graphite, and these findings were in line with the analysis of other previous characterization technique (Fig.5). Additionally, we could obtain more information from the XPS spectra of high-resolution. The $N1s$ spectrum could be separated into four curves at 397.6 eV, 398.9 eV, 403.4 eV, and 404.9eV, and they belonged to $C-N=C$, $N-(C)_3$, $C-N$, and π -excitation, respectively [62]. Also, the $Mo3p$ spectrum could be split into two peaks at 393.1eV and 394.6eV, which might belong to the $Mo3p_{1/2}$ and $Mo3p_{3/2}$. Besides, it was observed that $C1s$ spectrum displayed two obvious peaks from 282eV to 290eV, and the two curves could be separated into four curves at 283.5eV, 284.3eV, 287.3eV, and 288.4eV.

In addition, the peaks at 284.3eV were likely to be corresponded to C-C coordination of graphitic carbon atoms, and the peaks at 288.4eV could be ascribed to C-N or C-(N)₃ groups of aromatic ring in C₃N₄ [63]. Meanwhile, the peaks at 283.5eV and 287.3eV were probably attributed to C-C coordination of graphitic carbon atoms and C-C groups of the aromatic ring in graphite, respectively. In summary, the analytical results of N1s and C1s further proved the existence of

C₃N₄ and graphite. Moreover, the Mo3d_{3/2}, Mo3d_{5/2} and S_{2s} spectrum could be found at 231.9eV, 228.8eV, and 225.9eV, respectively. The appearance of Mo3d_{3/2}, Mo3d_{5/2}, Mo3p_{1/2}, and Mo3p_{3/2} might be attributed to the Mo⁴⁺ in MoS₂. Furthermore, The S2p spectrum could be observed that it was divided into two peaks at 162.8eV and 161.6eV, and the two peaks could be ascribed as S2p_{1/2} and S2p_{3/2}, which probably be corresponded to S²⁻ in MoS₂.

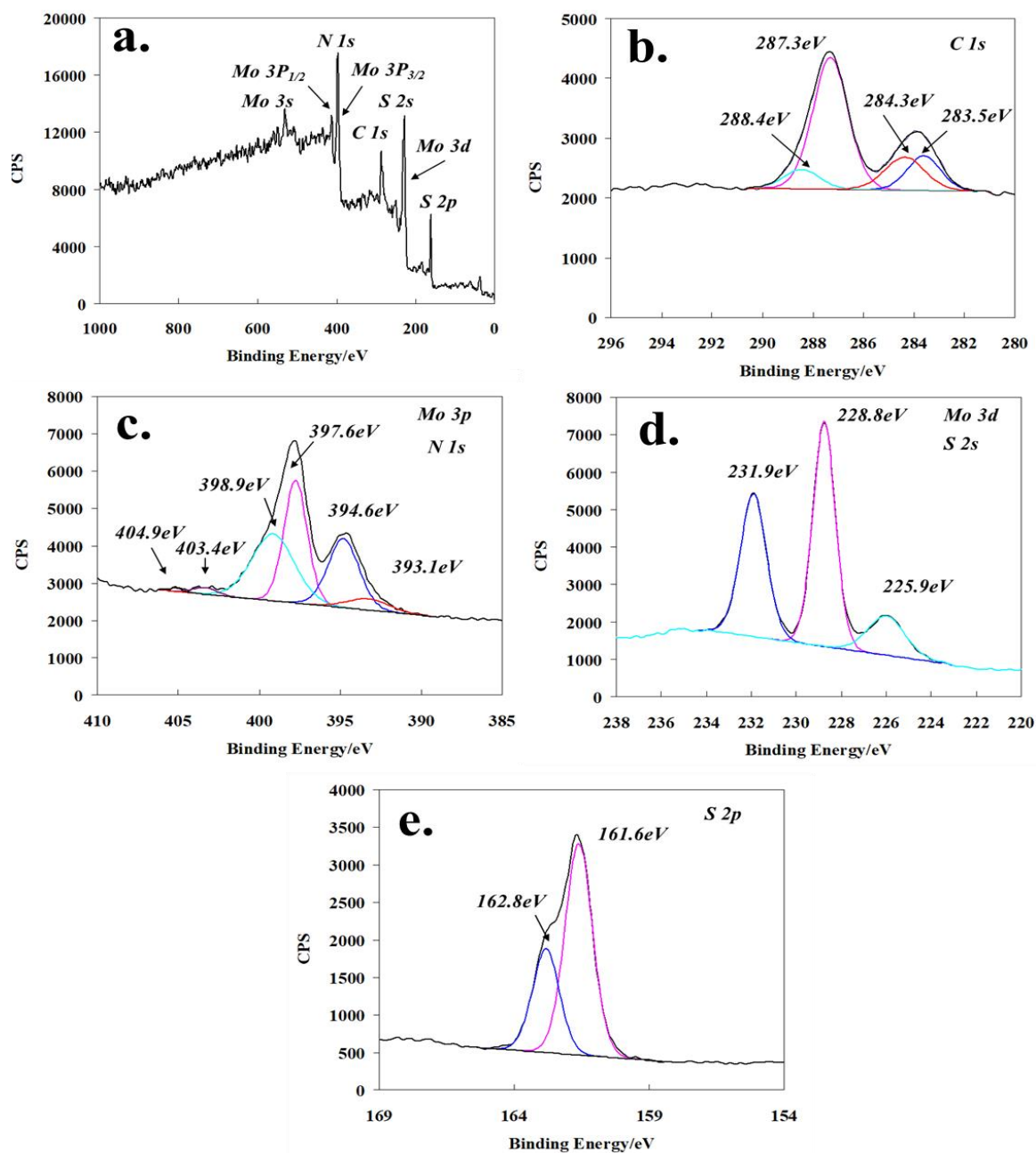


Fig. 6: The wide scan XPS spectra of MGC (a); the high-resolution XPS spectra of N1s and Mo 3p (b); C1s (c); Mo3d and S2s (d) and S2p (f).

TEM

Fig. 7 depicted the TEM and HRTEM results of MGC material. It was seen from Fig.7b and Fig.7c that, the 0.618nm interplanar spacing (in Fig.7b) and 0.336nm interplanar spacing (in Fig.7c) could be observed. Compared with the XRD analytical results of MGC, the 0.618nm and 0.336nm interplanar spacing might belong to the MoS_2 and

C_3N_4 . Moreover, we could clearly observe the cellular C atom sp_2 hybrid structure from Fig.7d, which indicated that this region was composed of graphite sheets. Combining the findings of Fig.7a to Fig.7d, the analytical results of TEM for MGC suggested that the nano-sized C_3N_4 (around 100nm) and MoS_2 particles (around 100nm) was loaded at the surface of flake graphite, which was consistent with the results of SEM.

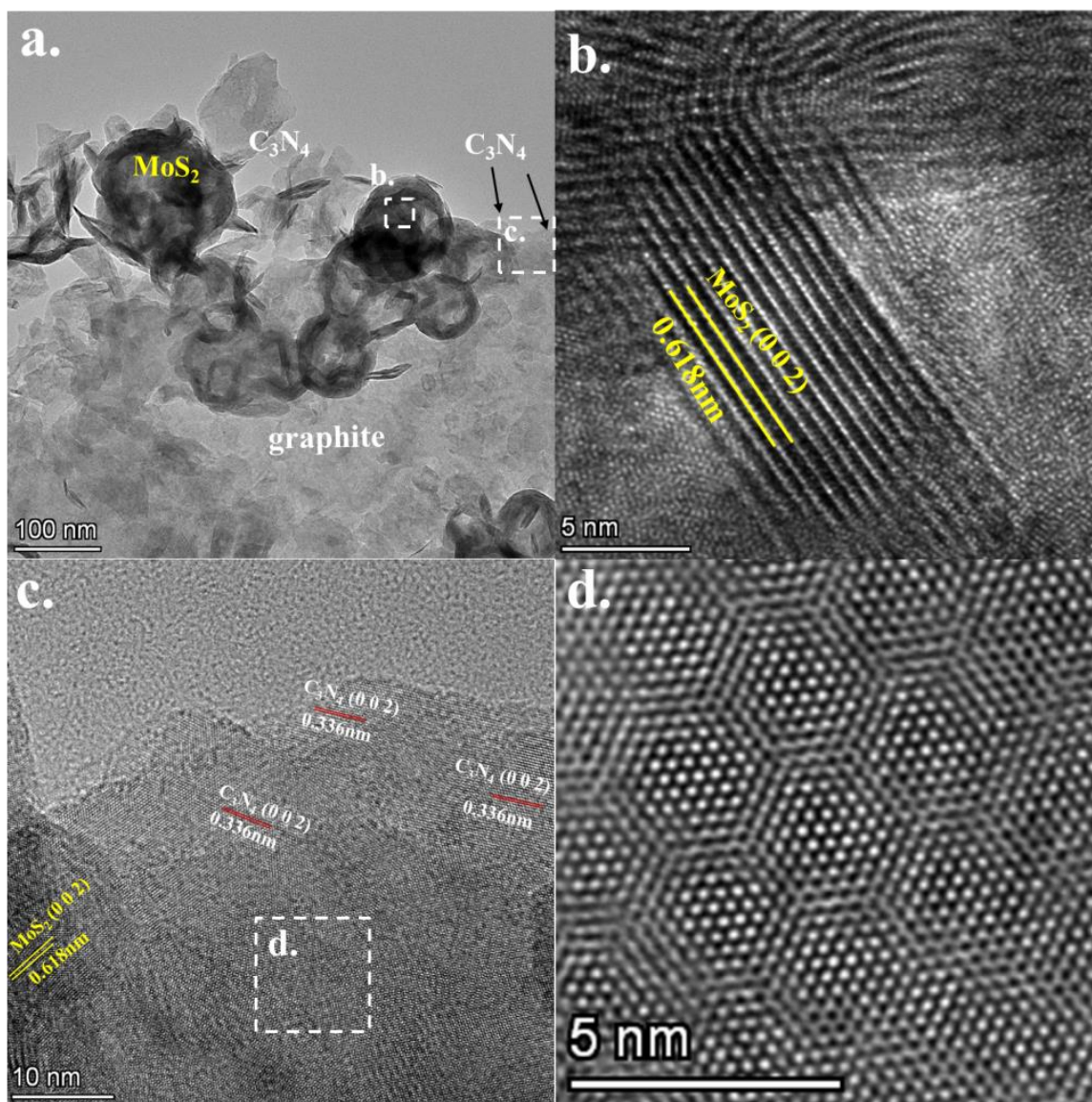


Fig. 7: The TEM image (a) and HRTEM image (b, c and d) of MGC material.

Photocatalytic performance

The photodegradation performances of catalysts were investigated through MB degradation under the condition of visible light in solution, as shown as Fig.8. Firstly, we studied the effect of catalyst dosages on the photodegradation efficiencies of MB. It was observed from Fig.8a that with the increase of catalyst dosages, the photodegradation efficiencies of pollutant increased gradually under the condition of visible light. In addition, with the same dosages of catalyst, MGC showed the highest photocatalytic degradation efficiencies compared with the other two catalysts (C_3N_4 and MoS_2). For example, when the dosage of catalyst was 1.0 g/L at 10min, the residual rate of MB was achieved at 27.3%. As an efficient photocatalyst, such photodegradation efficiency could be acceptable. The impact of reaction time on the photodegradation efficiencies was shown in Fig.8b. The period between -10 min to 0 min enhanced the uniform mixing of MB with catalysts. From the comparison of photocatalytic effect (Fig.8b), the addition of photocatalyst greatly accelerated the photodegradation of MB, and the removal rates of MB were much better than that of other two catalysts (C_3N_4 and MoS_2). For instance, the residual rate of MB was approximately 11.9% just at 20min after adding MGC catalyst, while the residual rate of MB were still 26.9% and 40.5% at 20min with MoS_2 and C_3N_4 as catalyst, respectively. Meanwhile, the catalytic degradation efficiencies of MoS_2 and C_3N_4 without illumination and only illumination without any catalyst were significantly lower than that of the normal photocatalytic reaction system, and the residual rate of MB were still 96.4%, 97.6%, and 98.5% at 30min, respectively. In contrast, the apparent degradation efficiencies of MB could be observed in MGC reaction system without light. These findings indicated that MGC catalyst had a certain degree of adsorption effect on MB, which was generally considered to be beneficial to the photocatalysis process. Besides, the changes of UV absorption spectra at visible light for MB at different reaction time were shown in Fig.8e. MB peaks were decreased with the reaction time gradually, which stated that MB displayed favorable photocatalytic degradation as adding MGC photocatalyst. Consequently, these findings demonstrated that the ternary composites (C_3N_4 , graphite, and MoS_2) greatly promoted the photocatalytic activity of MB.

Moreover, we investigated the apparent degradation kinetics via first-order reaction model, and the equation was seen as (2). The reaction constant of k could be gotten through plotting the experimental results via the equation (2).

$$\ln\left(\frac{C}{C_0}\right) = -kt \quad (2) [64]$$

where, C_0 represents MB initial concentration, and C_t represents MB concentration at time t

Fig.8c presented the fitting results of apparent kinetics utilizing the equation (2) (according on the experimental data in Fig.8b). According to the fitting results, the R^2 values of these three systems were all above 0.94, indicating that the photodegradation reaction for MB by these three catalysts could be suitably described through the reaction model of first-order. Additionally, the k value of MGC photodegradation system from Fig.8d was 0.0848, and that was the largest in these three systems.

Also, the morphology and XRD patterns of reused MGC after three times were also analyzed, as shown as Fig.9. It was seen that, the catalyst was basically maintained the initial morphology, and it was no obvious variations in the appearance of MGC material after the consecutive three times of photocatalysis experiment (Fig.9a). In addition, from XRD patterns of MGC material after 3rd of photocatalysis experiment (Fig.9b), it was found that the main curves of MoS_2 , C_3N_4 , and graphite could also be appeared contrast with the previous results. On the other hand, the decreasing peak intensity of graphite (2θ at 26.5°) could be observed, which means that there was a certain amount of graphite loss during the cycling process. At the same time, according to the reuse photodegradation curves of MGC (Fig.9c), there was only a slight reduction of photocatalytic activities after three cycles of recycle. These findings proved that MGC photocatalyst possessed remarkable photocatalytic stability, and the MGC photocatalyst could be efficiently reused.

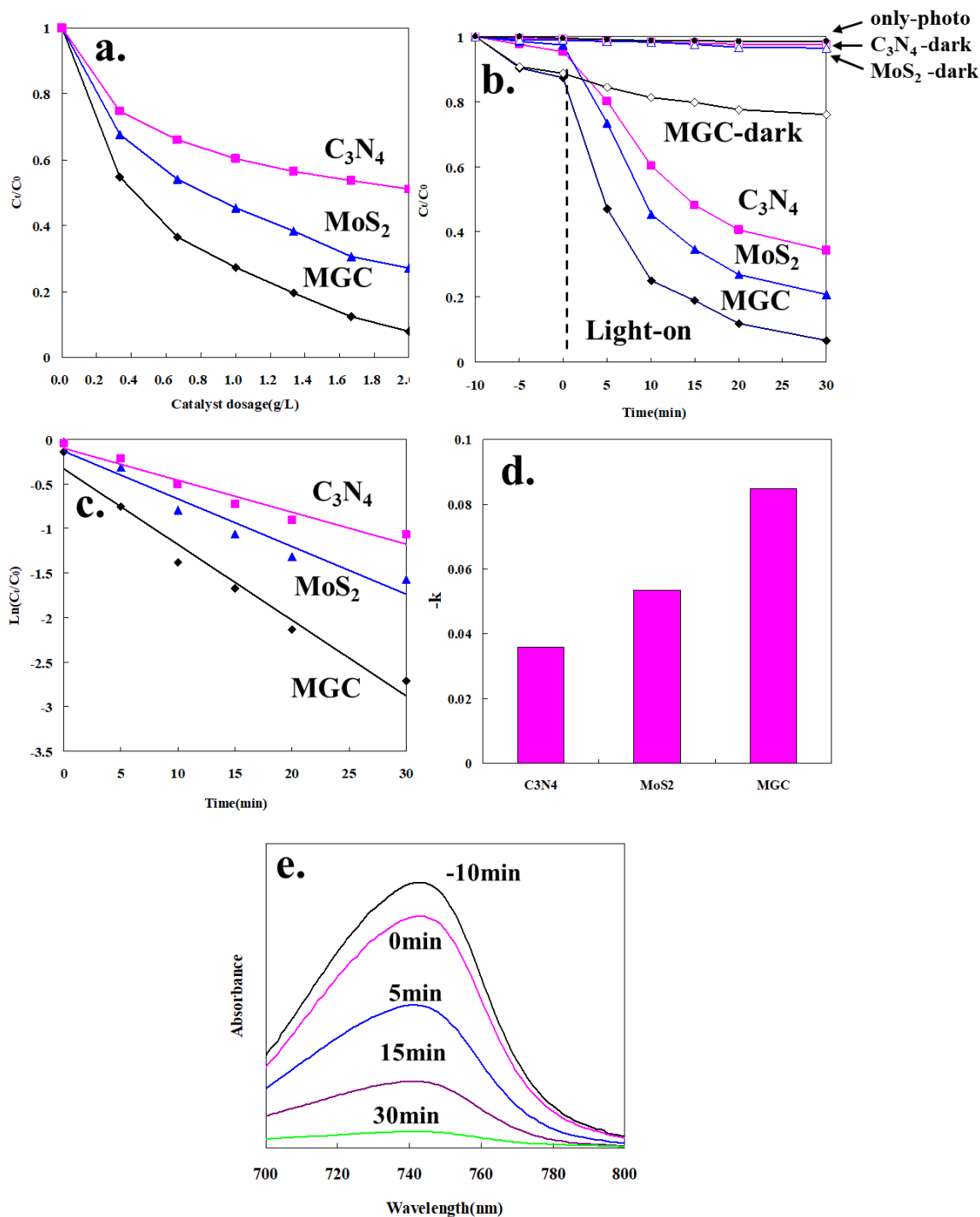


Fig. 8” (a) The impact of catalysts dosages on MB removal; (b) The photocatalytic degradation effect of catalyst under visible light, without visible light and only visible light; (c) the fitting findings utilizing the first-order model; (d) the constants in first-order reaction kinetics for the photodegradation of MB; (e) the absorption spectra of UV-visible for MB solution degraded by MGC Catalyst.

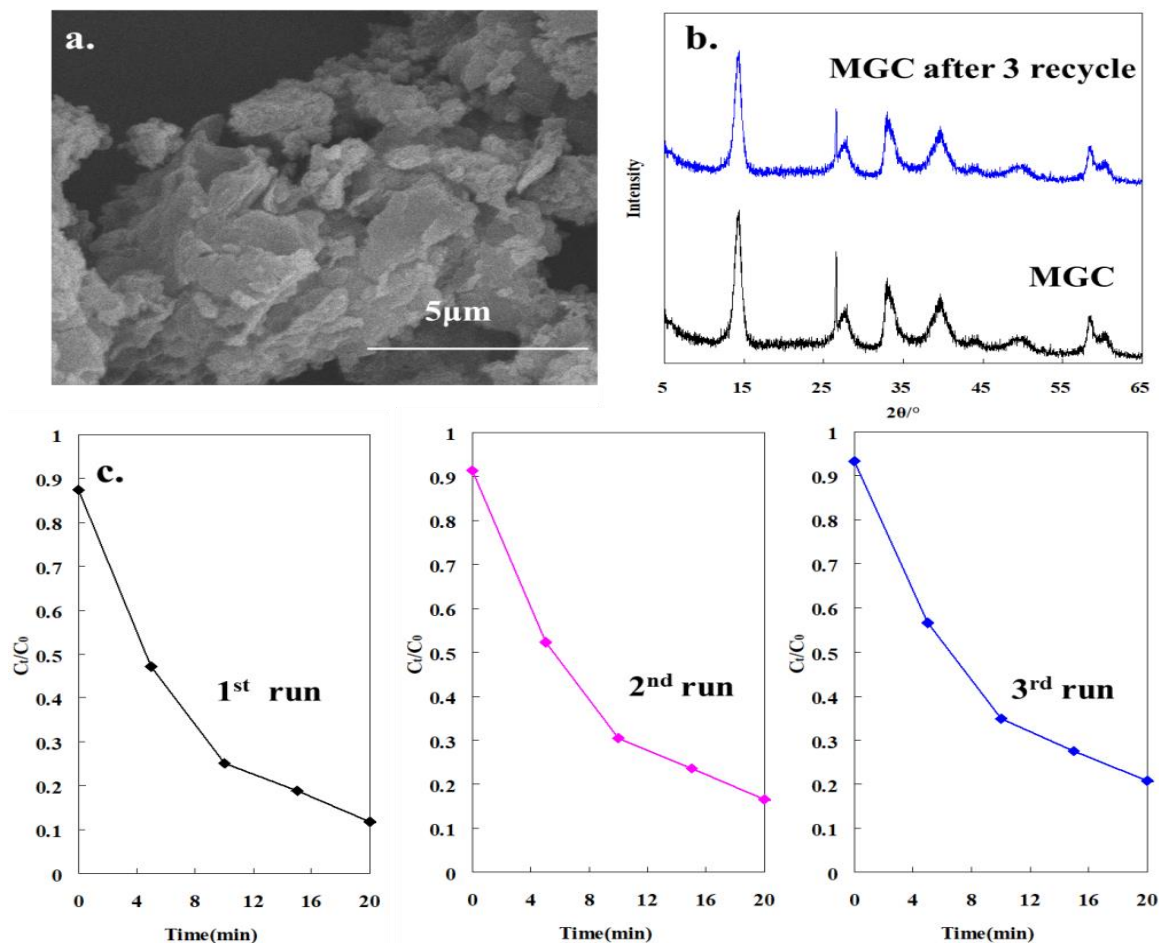


Fig. 9: (a) The morphology of MGC catalyst after 3rd photodegradation experiments; (b) The XRD patterns of MGC catalyst before and after 3rd photodegradation experiments; (c) the degradation curves of MGC catalyst reused under visible light.

Photocatalytic mechanism

The transient photocurrent response of MGC, MoS₂, and C₃N₄ under the irradiation of Xe lamp was described in Fig.10a. It was observed that sole MoS₂ and C₃N₄ appeared certain response, implying that MoS₂ and C₃N₄ were able to form many electrons and holes under the condition of visible light. Also, it was appeared that the photocurrent intensity of MGC photocatalytic material was improved greatly, confirming that MGC photocatalyst obtained stronger reflecting ability for the visible light. The highest photocurrent intensity also implied that the ternary composite (C₃N₄, graphite, and MoS₂) was helpful to the generation and transfer of photo-produced electrons and photo-produced holes.

Fig.10b depicted the EIS value of MGC, MoS₂, and C₃N₄. The radius values of MGC were the smallest, stating that the composite of materials could

reduce the resistance of charge transfer. This result was consistent with the previous phenomenon of Fig.3a, which could effectively promote the reaction process of photocatalysis. Additionally, the PL emission spectrum was carried out to investigate the combination and separation of photo-generated electrons and photo-generated holes, as shown in Fig.10c. It was found that the photoluminescence spectrum intensity of C₃N₄ was much higher than that of the other two catalysts. This finding indicated that the photo-induced electrons and holes produced by C₃N₄ had the greatest recombination possibility. Besides, the lower photoluminescence spectrum intensity of MoS₂ stated that the recombination possibility of electron and hole was lower than that of C₃N₄. And then, the MGC photocatalyst displayed the lowest photoluminescence spectrum intensity, suggesting that the composite of C₃N₄, graphite, and MoS₂ could further lead to the decrease of combination probability.

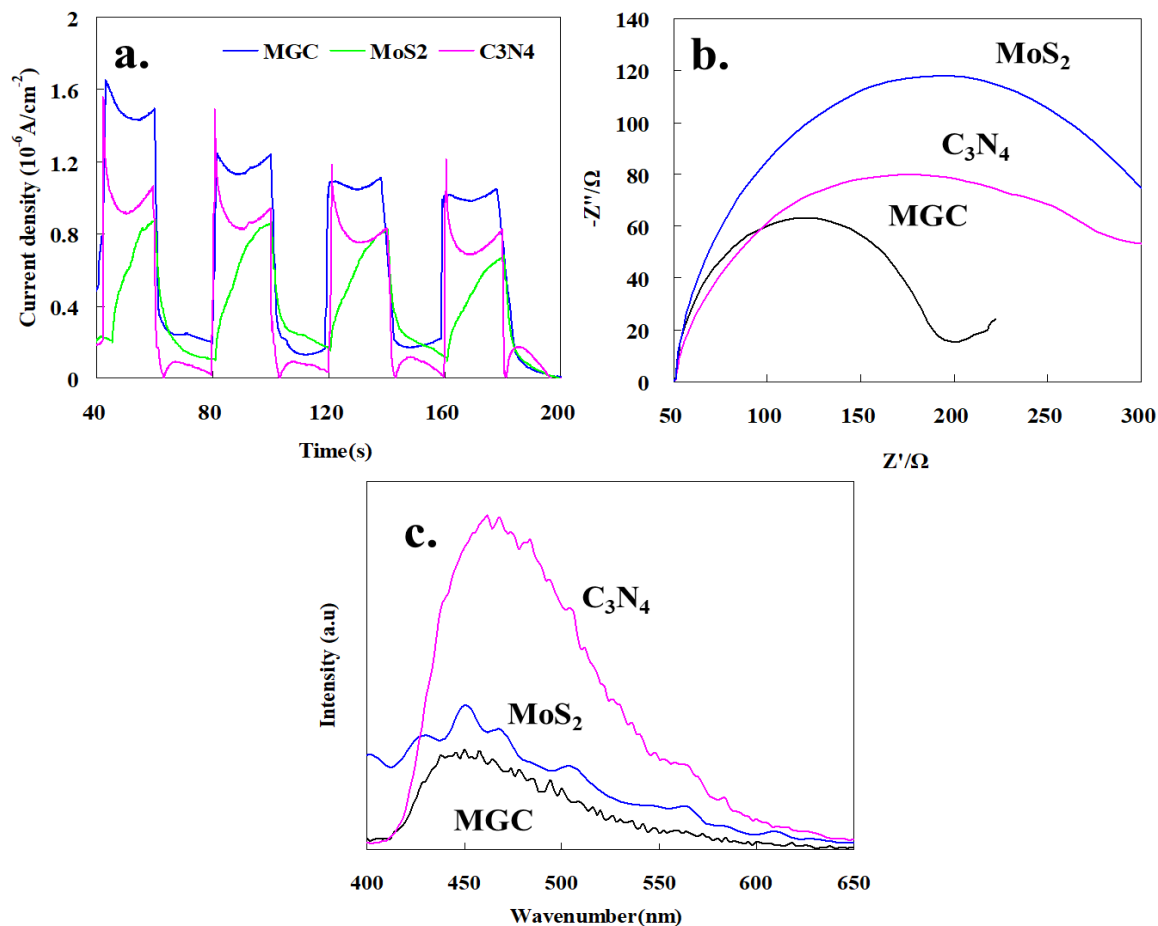


Fig. 10: Transient photocurrent responses (a), Electrochemical impedance spectra (b), and Steady-state PL spectra (c) of MGC, MoS₂, and C₃N₄.

To prove the active species in the photocatalytic process and clarify the action mechanism, the hydroxyl radicals (DMPO- \cdot OH) and the superoxide radicals (DMPO- \cdot O₂⁻) were detected using the DMPO technique by ESR spin-trapping spectra, as shown in Fig.11. There was no typical curves of \cdot OH or \cdot O₂⁻ were measured in MGC system as it was short of light system, implying that the exciting electrons and holes does not exist in the lack of visible light. In comparison, both typical curves of \cdot OH with the intensity ratio of 1:2:2:1 [65] and that of \cdot O₂⁻ [66] were measured under the irradiation of visible light, proving the active radicals of \cdot OH and \cdot O₂⁻ were generated in MGC photocatalytic process. Hence, the action process of these free reactive radicals might be one of the main photocatalytic mechanisms for the degradation of MB. Furthermore, to evaluate which species playing active roles during the course of photocatalytic degradation, the capturing agents were put into the mixtures to capture the active species. On the basis of related references [12, 13, 67], EDTA-2Na could be

utilized as a hole trapper, TBA could be utilized for a hydroxyl radical trapper, BQ could be considered as the free radical trapper of oxygen, and CCl₄ could be deemed as an electron trapper. Fig.11c depicted the impact of different types of capturing agents on the photodegradation efficiencies of MB. It was displayed that MB photodegradation efficiencies in MGC photocatalytic reaction systems were all descended when adding the capturing agents. This phenomenon verified that the photocatalytic activities of reaction systems were inhibited with the coexistent of these scavengers, and photocatalytic degradation path from equation (3) and (4) was probably happen during the degradation process. Also, it was found that both EDTA-2Na and TBA exhibited significant impacts on photodegradation process among these scavengers. These findings implied that the capturing of photo-produced holes and hydroxyl radicals was probably greatly lower the photocatalytic activities of reaction process, that might be interpreted by the main degradable pathway for MB as equation (5) and (6) by MGC catalyst in photocatalytic system.

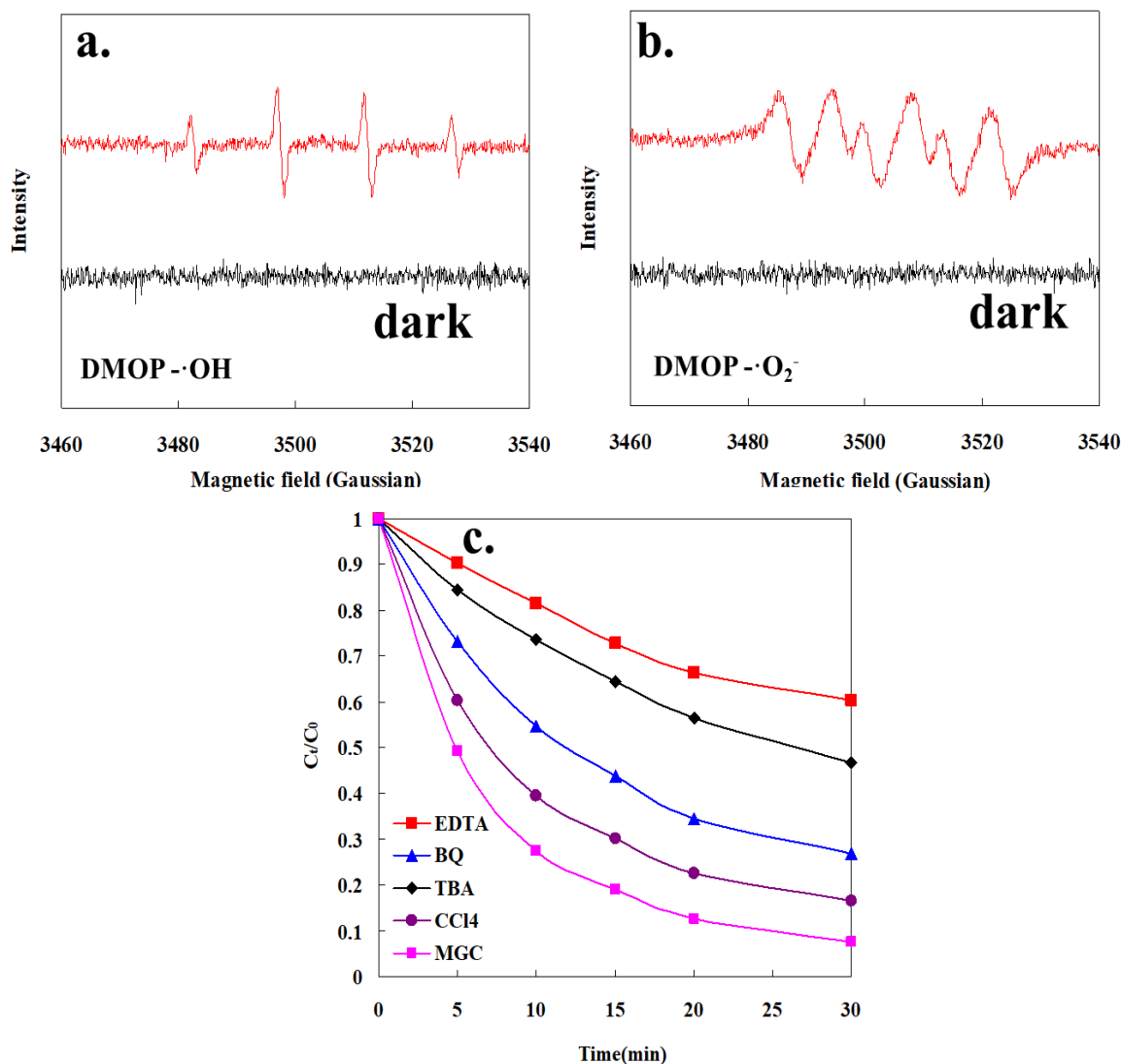


Fig. 11: ESR spectra of radical adducts trapped by DMPO in the dark and under the irradiation of visible light for DMPO•OH (a); ESR spectra of radical adducts trapped by DMPO in the dark and under the irradiation of visible light for DMPO•O₂⁻ (b); MB photocatalytic efficiencies after the addition of capturing agents (c).



Fig. 12 described the DFT calculation results of the energy bands for MoS₂, C₃N₄ and graphite. It was observed from Fig.12c that the band gap of graphite was 0, indicating that graphite was a conductive material, and that was consistent with our general understanding. In addition, it was appeared from Fig.12a and Fig.12b that the band gap value of

MoS₂ and C₃N₄ were 1.27eV and 1.56eV, respectively. The band gap values of both MoS₂ and C₃N₄ were both smaller than that of the experimental values in some degree, and the cause for this phenomenon is widely attributed to inherent defects in the DFT computational method. From the energy band structure and DOS results of MoS₂ and C₃N₄, it could be seen that the Fermi energy levels of both materials were approximated to the valence band top, indicating that MoS₂ and C₃N₄ were both p-type semiconductor materials theoretically.

Fig.13 displayed the work function of MoS₂, C₃N₄, and graphite from DFT calculation. It is well

known that when a p-type semiconductor meets a conductive material, electron transfer occurs between the two materials. In this research, since the work function of graphite was less than MoS₂, electrons would transfer from graphite to MoS₂ at the interface where MoS₂ contacted with graphite. When this process reached equilibrium, the Fermi level of MoS₂ and graphite was unified. In this case, the surface of graphite would be charged positive, while the surface of MoS₂ would be charged negative, thus forming a potential barrier from the graphite surface to MoS₂. This type of barrier would probably prevent the transfer of photo-induced holes generated by MoS₂ to the graphite. Meanwhile, it was likely that the barrier promoted the transfer of photo-induced electrons generated by MoS₂ to the graphite. Similarly, when the p-type C₃N₄ was gotten in touch with graphite, since the work function of C₃N₄ was far smaller than

that of the graphite, the potential barrier formed by the transfer of electrons and the unification of the Fermi level would prevent the photoelectrons generated by C₃N₄ transferring to the graphite. At the same time, it might promote the transfer of photo-induced holes generated by C₃N₄ to the graphite, as shown the photo-generated electrons and the photo-generated holes transfer path and photocatalysis mechanism in Fig.14. Furthermore, the two opposite barriers formed on the interface between graphite, MoS₂ and C₃N₄, would greatly enhance the division of photo-generated electrons and photo-generated holes in MoS₂ and C₃N₄, and reduce the recombination probability of photo-generated electrons and photo-generated holes, and thus greatly improve the photodegradation efficiencies of pollutants.

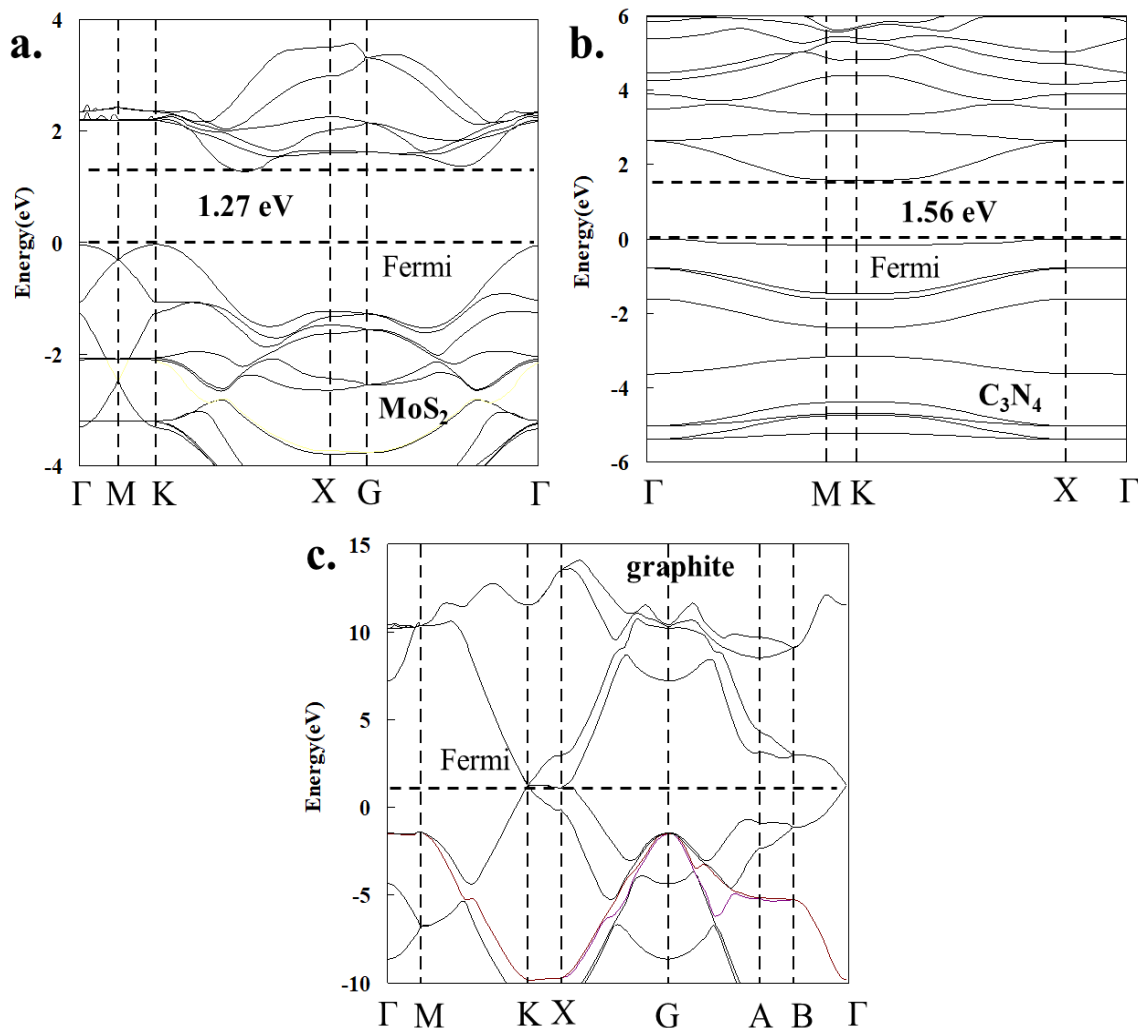


Fig. 12: Band structure of MoS₂, C₃N₄ and graphite from DFT calculation.

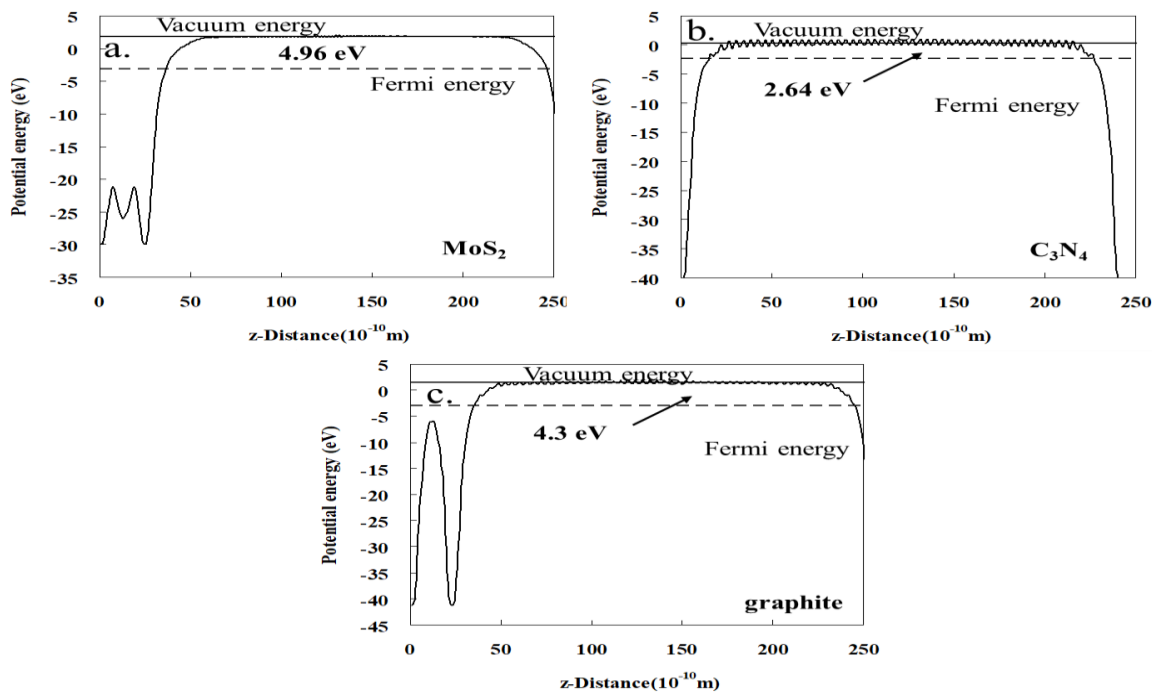


Fig. 13 The work function of MoS₂, C₃N₄ and graphite from DFT calculation.

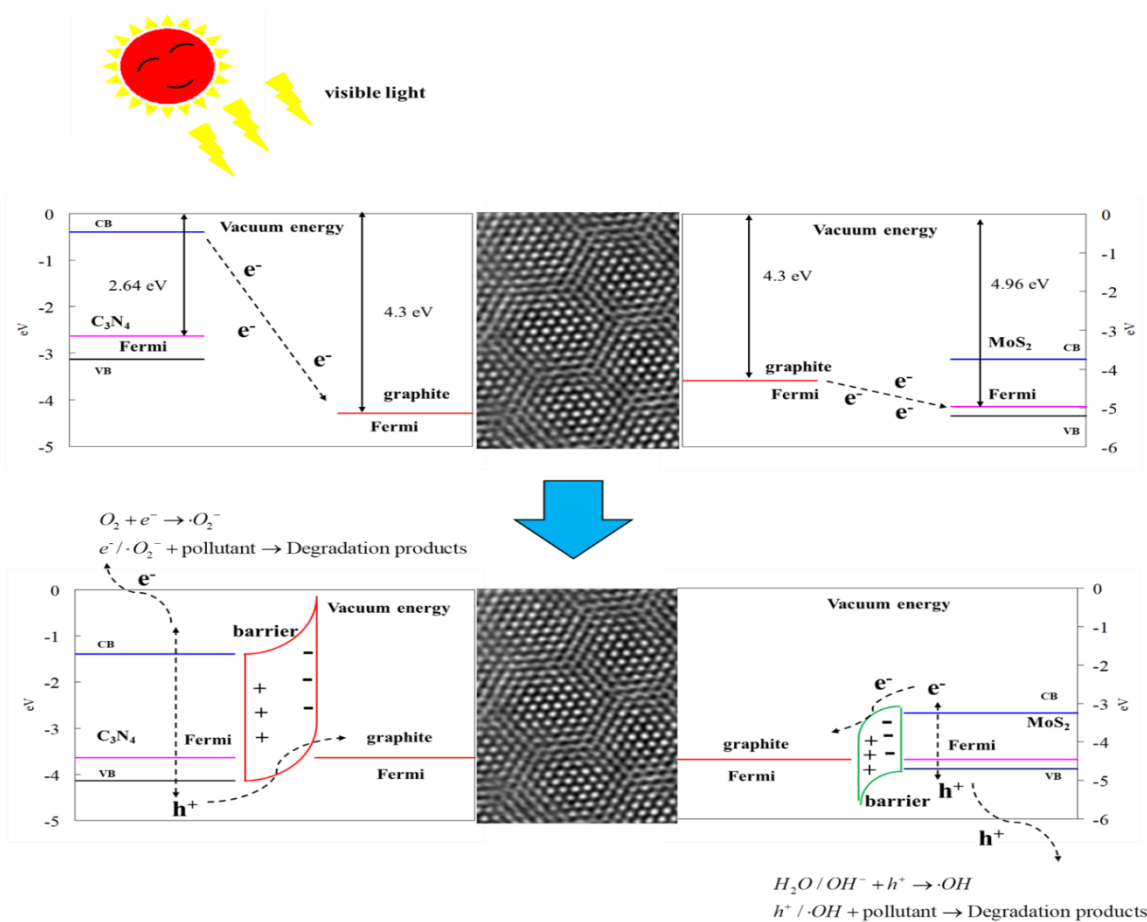


Fig. 14: Electron and hole transfer path and photocatalysis mechanism.

Conclusions

In this research, a MoS₂/graphite/C₃N₄ ternary photocatalytic material (MGC catalyst) was prepared and characterized by various modern instruments (including XRD, SEM-EDX, UV-Vis, XPS, ESR, EIS, and so on). In addition, the MGC material was applied to degrade MB, to investigate the photodegradation efficiencies under the visible light. Also, the DFT calculation was utilized to illustrate the photocatalytic mechanism of MGC catalyst for MB degradation. The characterization results demonstrated that MGC photocatalyst was a composite material of C₃N₄-graphite- MoS₂ ternary structure, and maintained lower band gap energy to obtain excellent visible light absorption efficiency. The photocatalytic experiments showed that, compared with C₃N₄ and MoS₂ catalyst, MGC displayed the highest degradation efficiencies among them, and it greatly promoted the photocatalytic activity of MB. Also, the photodegradation efficiencies of pollutant increased gradually as the increase of catalyst dosages, and the first-order reaction model could satisfactorily described the apparent photocatalytic degradation process of MB by these three catalysts. After the consecutive three times of photocatalysis experiments, MGC photocatalyst basically maintained the initial morphology, and possessed remarkable photocatalytic stability in the degradation activities of MB.

Moreover, the ternary composite structure of MGC was conducive to generate and transfer the photo-produced electrons and photo-produced holes. MGC photocatalyst displayed the lowest photoluminescence spectrum intensity, and the composite of C₃N₄, graphite, and MoS₂ further led to the decreasing of combination probability for photo-produced electrons and photo-produced holes. Additionally, the active radicals of •OH and •O₂⁻ producing in the photocatalytic reaction might play a crucial role to degrade MB. The DFT calculation results revealed that MoS₂ and C₃N₄ were both p-type semiconductor materials theoretically; on the interface between graphite, MoS₂ and C₃N₄, the two opposite barriers were formed, and that would significantly accelerate the division of photo-produced electrons and photo-produced holes in MoS₂ and C₃N₄; hence, it might reduce the recombination probability of photo-produced electrons and photo-produced holes, and then effectively enhance the photodegradation efficiencies of the target pollutant.

Acknowledgements

This work is supported by Science Foundation of Jiangsu Colleges and Universities (Grant No. 17KJD610001, 17KJD610002), Zhenjiang City 2021 key research and development project (Social Development) under Grant (SH2021020), 2021 Jiangsu Province University Students Innovation and Entrepreneurship Training Program Project (202114000015Y); Jiangsu Open University School-level Scientific Research Institutions.

Reference

1. J.J. Rueda-Marquez, I. Levchuk, P.F. Ibanez, M. Sillanpaa, A critical review on application of photocatalysis for toxicity reduction of real wastewaters, *J Clean Prod*, **258**, 13, (2020).
2. D.J. Chen, Y.L. Cheng, N. Zhou, P. Chen, Y.P. Wang, K. Li, S.H. Huo, P.F. Cheng, P. Peng, R.C. Zhang, L. Wang, H. Liu, Y.H. Liu, R. Ruan, Photocatalytic degradation of organic pollutants using TiO₂-based photocatalysts: A review, *J Clean Prod*, **268**, 121725, (2020).
3. C. Grandclement, I. Seyssiecq, A. Piram, P. Wong-Wah-Chung, G. Vanot, N. Tiliacos, N. Roche, P. Doumenq, From the conventional biological wastewater treatment to hybrid processes, the evaluation of organic micropollutant removal: A review, *Water Res*, **111**, 297, (2017).
4. M. Ikram, M. Zahoor, E. Khan, S.M.U. Khayam, Biodegradation of Novacron Turquoise (Reactive Blue 21) by *Pseudomonas aeruginosa*, *J Chem Soc Pakiatan*, **42**, 737, (2020).
5. C.S. Lee, J. Robinson, M.F. Chong, A review on application of flocculants in wastewater treatment, *Process Saf. Environ. Protect.*, **92**, 489, (2014).
6. I. Ali, A. Basheer, X.Y. Mbianda, A. Burakov, E. Galunin, I. Burakova, E. Mkrtychyan, A. Tkachev, V. Grachev, Graphene based adsorbents for remediation of noxious pollutants from wastewater, *Environ. Int.*, **127**, 160, (2019).
7. T. Cheng, C. Chen, R. Tang, C.-H. Han, Y. Tian, Competitive Adsorption of Cu, Ni, Pb, and Cd from Aqueous Solution Onto Fly Ash-Based Linde F(K) Zeolite, *Iran J Chem Eng*, **37**, 61, (2018).
8. C. Chen, T. Cheng, X. Zhang, R. Wu, Q. Wang, Synthesis of an Efficient Pb Adsorption Nano-Crystal under Strong Alkali Hydrothermal Environment Using a Gemini Surfactant as Directing Agent, *J Chem Soc Pakiatan*, **41**, 1034, (2019).

9. E.O. Ezugbe, S. Rathilal, Membrane Technologies in Wastewater Treatment: A Review, *Membranes*, **10**, 28, (2020).
10. B. Bethi, S.H. Sonawane, B.A. Bhanvase, S.P. Gumfekar, Nanomaterials-based advanced oxidation processes for wastewater treatment: A review, *Chem. Eng. Process.*, **109**, 178, (2016).
11. S. Islam, I.A. Shaikh, N. Firdous, A. Ali, Y. Sadef, Performance Evaluation of Fenton Oxidation Treatment Method for the Reuse of Reactive Dyeing Effluent, *J Chem Soc Pakiatan*, **41**, 1138, (2019).
12. T. Cheng, C. Chen, L. Wang, X. Zhang, C. Ye, Q. Deng, G. Chen, Synthesis of Fly Ash Magnetic Glass Microsphere@BiVO₄ and Its Hybrid Action of Visible-Light Photocatalysis and Adsorption Process, *Pol J Environ Stud*, **30**, 2027, (2021).
13. C. Chen, L. Wang, T. Cheng, X. Zhang, Z. Zhou, X. Zhang, Q. Xu, Ag₃PO₄/AgSbO₃ composite as novel photocatalyst with significantly enhanced activity through a Z-scheme degradation mechanism, *J Iran Chem Soc*, (2021).
14. Q. Zeng, S. Chang, A. Beyhaqi, M. Wang, C. Hu, Efficient electricity production coupled with water treatment via a highly adaptable, successive water-energy synergistic system, *Nano Energy*, **67**, 104237, (2019).
15. Q. Zeng, S. Chang, M. Wang, M. Li, Q.W. Deng, Z. Xiong, Z.Y. Liu, Highly-active, metal-free, carbon-based ORR cathode for efficient organics removal and electricity generation in a PFC system, *Chinese Chem Lett*, **32**, 2212, (2021).
16. C. Chen, T. Cheng, Wet Air Oxidation and Catalytic Wet Air Oxidation for Refinery Spent Caustics Degradation, *J Chem Soc Pakiatan*, **35**, 243, (2013).
17. C. Chen, T. Cheng, L. Wang, Y. Tian, Q. Deng, Y. Shi, Application of MoO₃ as an efficient catalyst for wet air oxidation treatment of pharmaceutical wastewater (Experimental and DFT study), *Arch Environ Prot*, **47**, 47, (2021).
18. Y. Feng, L. Yang, J. Liu, B.E. Logan, Electrochemical technologies for wastewater treatment and resource reclamation, *Environ Sci-Wat Res*, **2**, 800, (2016).
19. S. Garcia-Segura, J.D. Ocon, M.N. Chong, Electrochemical oxidation remediation of real wastewater effluents - A review, *Process Saf. Environ. Protect.*, **113**, 48, (2018).
20. Y. Liu, Y. Zhao, J.L. Wang, Fenton/Fenton-like processes with in-situ production of hydrogen peroxide/hydroxyl radical for degradation of emerging contaminants: Advances and prospects, *J Hazard Mater*, **404**, 124191, (2021).
21. M.H. Zhang, H. Dong, L. Zhao, D.X. Wang, D. Meng, A review on Fenton process for organic wastewater treatment based on optimization perspective, *Sci. Total Environ.*, **670**, 110, (2019).
22. S. Zhang, B. Li, X. Wang, G. Zhao, B. Hu, Z. Lu, T. Wen, J. Chen, X. Wang, Recent developments of two-dimensional graphene-based composites in visible-light photocatalysis for eliminating persistent organic pollutants from wastewater, *Chem Eng J*, **390**, 124642, (2020).
23. W.S. Koe, J.W. Lee, W.C. Chong, Y.L. Pang, L.C. Sim, An overview of photocatalytic degradation: photocatalysts, mechanisms, and development of photocatalytic membrane, *Environ Sci Pollut R*, **27**, 2522, (2020).
24. H. An Bai, Z. Chen, C. Li, J. Wan, Preparation of a Nanocomposite Photocatalyst and its Application in Dye Wastewater Treatment, *J Chem Soc Pakiatan*, **40**, 399, (2018).
25. Q. Wang, Q. Gao, A.M. Al-Enizi, A. Nafady, S. Ma, Recent advances in MOF-based photocatalysis: environmental remediation under visible light, *Inorg Chem Front*, **7**, 300, (2020).
26. L. Pan, S. Sun, Y. Chen, P. Wang, J. Wang, X. Zhang, J.-J. Zou, Z.L. Wang, Advances in Piezo-Phototronic Effect Enhanced Photocatalysis and Photoelectrocatalysis, *Adv Energy Mater*, **10**, 2000214, (2020).
27. Z.Q. Long, Q.G. Li, T. Wei, G.M. Zhang, Z.J. Ren, Historical development and prospects of photocatalysts for pollutant removal in water, *J Hazard Mater*, **395**, 122599, (2020).
28. Y.P. Wang, H. Yang, X.F. Sun, H.M. Zhang, T. Xian, Preparation and photocatalytic application of ternary n-BaTiO₃/Ag/p-AgBr heterostructured photocatalysts for dye degradation, *Mater Res Bull*, **124**, 110754, (2020).
29. H.J. Gao, X.X. Zhao, H.M. Zhang, J.F. Chen, S.F. Wang, H. Yang, Construction of 2D/0D/2D Face-to-Face Contactg-C₃N₄@Au@Bi(4)Ti(3)O(12)Heterojunction Photocatalysts for Degradation of Rhodamine B, *J Electron Mater*, **49**, 5248, (2020).
30. K. Wang, Z. Xing, D. Meng, S. Zhang, W. Zhou, Hollow MoSe₂@Bi₂S₃/CdS Core-Shell Nanostructure as Dual Z-Scheme Heterojunctions with Enhanced Full Spectrum Photocatalytic-Photothermal Performance, *Appl Catal B-Environ*, **281**, 119482, (2020).
31. D. Zhu, Q. Zhou, Nitrogen doped g-C₃N₄ with the extremely narrow band gap for excellent photocatalytic activities under visible light, *Appl*

- Catal B-Environ, **281**, 119474, (2020).
32. C. Chen, L. Wang, T. Cheng, X. Zhang, Y.S. Shi, Silver Doped Sodium Antimonate with Greatly Reduced the Band Gap for Efficiently Enhanced Photocatalytic Activities Under Visible Light (Experiment and DFT Calculation), *Mater Res-Ibero-Am J*, **24**, e20210100, (2021).
 33. Q. Guo, Z. Ma, C. Zhou, Z. Ren, X. Yang, Single Molecule Photocatalysis on TiO₂ Surfaces, *Chem Rev*, **119**, 11020, (2019).
 34. Q. Guo, C. Zhou, Z. Ma, X. Yang, Fundamentals of TiO₂ Photocatalysis: Concepts, Mechanisms, and Challenges, *Adv Mater*, **31**, 1901997, (2019).
 35. F.Y. Chen, Y.M. Liu, X. Zhang, L.N. He, Y.B. Tang, Inorganic-Framework Molecularly Imprinted CdS/TiO₂ for Selectively Photocatalytic Degradation of Di (2-ethylhexyl) phthalate, *J Chem Soc Pakiatan*, **41**, 308, (2019).
 36. S.G. Kumar, K.S.R.K. Rao, Zinc oxide based photocatalysis: tailoring surface-bulk structure and related interfacial charge carrier dynamics for better environmental applications, *Rsc Adv*, **5**, 3306, (2015).
 37. K. Qi, B. Cheng, J. Yu, W. Ho, Review on the improvement of the photocatalytic and antibacterial activities of ZnO, *J Alloy Compd*, **727**, 792, (2017).
 38. W. Feng, M. Tao, P. Huang, Controllable Tuning Various Ratios of ZnO Materials Polar Facets in Dimethylacetamide Media and their Kinetic Photocatalytic Activity, *J Chem Soc Pakiatan*, **40**, 263, (2018).
 39. J. Akhtar, M.B. Tahir, M. Sagir, H.S. Bamufleh, Improved photocatalytic performance of Gd and Nd co-doped ZnO nanorods for the degradation of methylene blue, *Ceram Int*, **46**, 11955, (2020).
 40. A. Malathi, J. Madhavan, M. Ashokkumar, P. Arunachalam, A review on BiVO₄ photocatalyst: Activity enhancement methods for solar photocatalytic applications, *Appl Catal A-Gen*, **555**, 47, (2018).
 41. M.A. Wahba, S.M. Yakout, W.A.A. Mohamed, H.R. Galal, Remarkable photocatalytic activity of Zr doped ZnO and ZrO₂/ZnO nanocomposites: Structural, morphological and photoluminescence properties, *Mater Chem Phys*, **256**, 123754, (2020).
 42. L.M. Castro Honorio, A.L. Menezes de Oliveira, E.C. da Silva Filho, J.A. Osajima, A. Hakki, D.E. Macphee, I.M. Garcia dos Santos, Supporting the photocatalysts on ZrO₂: An effective way to enhance the photocatalytic activity of SrSnO₃, *Appl Surf Sci*, **528**, 146991, (2020).
 43. Q. Li, X. Li, S. Wageh, A.A. Al-Ghamdi, J.G. Yu, CdS/Graphene Nanocomposite Photocatalysts, *Adv Energy Mater*, **5**, 1500010, (2015).
 44. X.F. Ning, G.X. Lu, Photocorrosion inhibition of CdS-based catalysts for photocatalytic overall water splitting, *Nanoscale*, **12**, 1213, (2020).
 45. N. Rono, J.K. Kibet, B.S. Martincigh, V.O. Nyamori, A review of the current status of graphitic carbon nitride, *Crit Rev Solid State*, **46**, 189, (2021).
 46. S.W. Cao, J.X. Low, J.G. Yu, M. Jaroniec, Polymeric Photocatalysts Based on Graphitic Carbon Nitride, *Adv Mater*, **27**, 2150, (2015).
 47. N.S. Alhokbany, R. Mousa, M. Naushad, S.M. Alshehri, T. Ahamad, Fabrication of Z-scheme photocatalysts g-C₃N₄/Ag₃PO₄/chitosan for the photocatalytic degradation of ciprofloxacin, *Int J Biol Macromol*, **164**, 3864, (2020).
 48. D.Z. Lu, H.M. Wang, X.N. Zhao, K.K. Kondamareddy, J.Q. Ding, C.H. Li, P.F. Fang, Highly Efficient Visible-Light-Induced Photoactivity of Z-Scheme g-C₃N₄/Ag/MoS₂ Ternary Photocatalysts for Organic Pollutant Degradation and Production of Hydrogen, *Acc Sustain Chem Eng*, **5**, 1436, (2017).
 49. Q. Li, N. Zhang, Y. Yang, G.Z. Wang, D.H.L. Ng, High Efficiency Photocatalysis for Pollutant Degradation with MoS₂/C₃N₄ Heterostructures, *Langmuir*, **30**, 8965, (2014).
 50. Y.X. Fu, Y. Li, T.L. Chang, X.T. Liu, X.F. Wu, J.R. Zhang, H. Wang, X.Y. Ma, Synthesis and Characterization of WO₃ center dot 0.33H₂O/Ag₂MoO₄ Composites as a Visible-Light-Driven Photocatalyst for Rhodamine B and Levofloxacin Degradation, *J Chem Soc Pakiatan*, **42**, 827, (2020).
 51. A. Beyhaqi, Q. Zeng, S. Chang, M. Wang, C. Hu, Construction of g-C₃N₄/WO₃/MoS₂ ternary nanocomposite with enhanced charge separation and collection for efficient wastewater treatment under visible light, *Chemosphere*, **247**, 125784, (2020).
 52. S. Horikoshi, N. Serpone, Can the photocatalyst TiO₂ be incorporated into a wastewater treatment method? Background and prospects, *Catal Today*, **340**, 334, (2020).
 53. J.W. Fu, J.G. Yu, C.J. Jiang, B. Cheng, g-C₃N₄-Based Heterostructured Photocatalysts, *Adv Energy Mater*, **8**, 1701503, (2018).
 54. F. He, Z.X. Wang, Y.X. Li, S.Q. Peng, B. Liu, The nonmetal modulation of composition and morphology of g-C₃N₄-based photocatalysts, *Appl Catal B-Environ*, **269**, 118828, (2020).
 55. C. Prasad, H. Tang, Q.Q. Liu, I. Bahadur, S. Karlapudi, Y.J. Jiang, A latest overview on

- photocatalytic application of g-C₃N₄ based nanostructured materials for hydrogen production, *Int J Hydrogen Energ*, **45**, 337, (2020).
56. B. Chen, Y.H. Meng, J.W. Sha, C. Zhong, W.B. Hua, N.Q. Zhao, Preparation of MoS₂/TiO₂ based nanocomposites for photocatalysis and rechargeable batteries: progress, challenges, and perspective, *Nanoscale*, **10**, 34, (2018).
 57. X. Zhang, Z.C. Lai, C.L. Tan, H. Zhang, Solution-Processed Two-Dimensional MoS₂ Nanosheets: Preparation, Hybridization, and Applications, *Angew Chem Int Edit*, **55**, 8816, (2016).
 58. J.X. Low, C. Jiang, B. Cheng, S. Wageh, A.A. Al-Ghamdi, J.G. Yu, A Review of Direct Z-Scheme Photocatalysts, *Small Methods*, **1**, 1700080, (2017).
 59. B.J. Ng, L.K. Putri, X.Y. Kong, Y.W. Teh, P. Pasbakhsh, S.P. Chai, Z-Scheme Photocatalytic Systems for Solar Water Splitting, *Adv Sci*, **7**, 1903171, (2020).
 60. X. Huang, F. Guo, M. Li, H. Ren, Y. Shi, L. Chen, Hydrothermal synthesis of ZnSnO₃ nanoparticles decorated on g-C₃N₄ nanosheets for accelerated photocatalytic degradation of tetracycline under the visible-light irradiation, *Sep Purif Technol*, **230**, 115854, (2020).
 61. T. Ma, X.Q. Xia, C.B. Liu, F. Tang, T. Jin, J.C. Qian, Z.G. Chen, Preparation of MoS₂-Ag/g-C₃N₄ Composite for Rhodamine B Degradation, *Nano*, **16**, 2150078, (2021).
 62. F. Guo, W.L. Shi, M.Y. Li, Y. Shi, H.B. Wen, 2D/2D Z-scheme heterojunction of CuInS₂/g-C₃N₄ for enhanced visible-light-driven photocatalytic activity towards the degradation of tetracycline, *Sep Purif Technol*, **210**, 608, (2019).
 63. F. Guo, M.Y. Li, H.J. Ren, X.L. Huang, K.K. Shu, W.L. Shi, C.Y. Lu, Facile bottom-up preparation of Cl-doped porous g-C₃N₄ nanosheets for enhanced photocatalytic degradation of tetracycline under visible light, *Sep Purif Technol*, **228**, 115770, (2019).
 64. D. Zhu, Q. Zhou, Nitrogen doped g-C₃N₄ with the extremely narrow band gap for excellent photocatalytic activities under visible light, *Appl Catal B-Environ*, **281**, 119474, (2021).
 65. W. Zhao, Y. Li, P. Zhao, L. Zhang, B. Dai, J. Xu, H. Huang, Y. He, D.Y.C. Leung, Novel Z-scheme Ag-C₃N₄/SnS₂ plasmonic heterojunction photocatalyst for degradation of tetracycline and H₂ production, *Chem Eng J*, **405**, 126555, (2021).
 66. F. Chen, Q. Yang, X. Li, G. Zeng, D. Wang, C. Niu, J. Zhao, H. An, T. Xie, Y. Deng, Hierarchical assembly of graphene-bridged Ag₃PO₄/Ag/BiVO₄ (040) Z-scheme photocatalyst: An efficient, sustainable and heterogeneous catalyst with enhanced visible-light photoactivity towards tetracycline degradation under visible light irradiation, *Appl Catal B-Environ*, **200**, 330, (2017).
 67. C. Du, J. Song, S. Tan, L. Yang, G. Yu, H. Chen, L. Zhou, Z. Zhang, Y. Zhang, Y. Su, X. Wen, S. Wang, Facile synthesis of Z-scheme ZnO/Ag/Ag₃PO₄ composite photocatalysts with enhanced performance for the degradation of ciprofloxacin, *Mater Chem Phys*, **260**, 124136, (2021).